Arbitrary-Order Conservative and Consistent Remapping and a Theory of Linear Maps, Part 1

Paul A. Ullrich*

Department of Land, Air and Water Resources, University of California, Davis, California

Mark A. Taylor

Sandia National Laboratories, Albuquerque, New Mexico

Corresponding author address: Paul Ullrich, Department of Land, Air and Water Resources, University of California, Davis, 1 Shields Avenue, Davis, California 95616.

E-mail: paullrich@ucdavis.edu

ABSTRACT

The design of accurate, conservative, consistent and monotone operators for remapping scalar fields between computational grids on the sphere has been a persistent issue for global modeling groups. This problem is especially pronounced when mapping between distinct discretizations (such as finite volumes or finite elements). To this end, this paper provides a novel unified mathematical framework for the development of linear remapping operators. This framework is then applied in the development of high-order conservative, consistent and monotone linear remapping operators from a finite element discretization to a finite volume discretization. The resulting scheme is evaluated in the context of both idealized and operational simulations and shown to perform well for a variety of problems.

1. Introduction

The unique characteristics of the atmosphere, ocean and land surface have led the global modeling community to design component models with distinct numerical methods and meshes. Increasingly there has been a further push towards using different numerical meshes for particular physical processes in order to improve accuracy and efficiency of the modeling system. In either case, some mechanism for communication between these meshes is necessary to couple these components and allow for proper accounting of globally conserved quantities. Consequently, the design of conservative, consistent and monotone remapping operators for translating between different computational grids on the sphere (hereafter referred to as the *remapping problem*), has been a persistent issue for global modeling groups.

This manuscript is the first in a series describing the new TempestRemap software package for accurate remapping between meshes on the sphere. Remapping operators are usually constructed via a two-stage process: First a search algorithm determines which regions on the source mesh are geometrically "close" to regions on the target mesh. This procedure is performed to ensure that the mapping maintains geometrical locality. Second, a mapping is defined between source regions and target regions which accounts for sub-grid-scale variation of the source field. See, for example, Jones (1999); Margolin and Shashkov (2003); Ullrich et al. (2009); Farrell et al. (2009); Farrell and Maddison (2011); Dong and Wang (2013).

A robust search algorithm can be particularly difficult to define, since special cases such as coincident grid lines, small overlap regions and the non-linearity of spherical geometry can quickly lead to conditioning issues. The search problem can be simplified by using dimension splitting to approximate overlap regions (Lauritzen and Nair 2007), restricting the choice of source and target meshes (Ullrich et al. 2009), or by using approximations to grid lines (Jones 1999). The

implementation of TempestRemap described in this paper follows the Earth System Modeling Framework (Hill et al. 2004) by restricting the geometry to meshes composed exclusively of regions whose edges consist of great circle arcs, although there are future plans for supporting grid lines of constant latitude.

Non-conservative mapping operators are generally easy to construct using bilinear interpolation (if monotonicity preservation is required) or high-order finite-differencing techniques. However, these operations are not well suited for arbitrary resolution source and target meshes, and when used in conjunction with *ad hoc* global conservation fixers can produce strange non-localized behavior. To define a conservative mapping operator, a common approach has been to use the Gauss-Green theorem (Dukowicz and Kodis 1987) to transform area integrals into line integrals around the boundary of the integration region. This approach has been successfully applied for the conservative remapping problem in the Spherical Coordinate Remapping and Interpolation Package (Jones 1999, SCRIP), and was later used by Ullrich et al. (2009) to define a geometrically exact remapping operator between cubed-sphere and regular latitude-longitude meshes. Unfortunately, the use of the Gauss-Green theorem requires that an analytical potential function be found that accounts for the underlying geometry. This is generally only possible for certain simple cases, and is particularly difficult on completely unstructured meshes. To overcome this problem, Erath et al. (2013) instead proposed using a non-conservative remapping operator defined from inexact area integration via quadrature which was then re-scaled to produce a conservative operator. This approach avoided the ill-conditioning that arose at higher spatial resolutions from line-integral approach (Ullrich et al. 2013), but led to a loss of consistency of the remapping operator. In order to overcome this problem TempestRemap uses a quadrature-based approach to produce a "first guess" operator which is then projected onto the space of conservative and consistent solutions using a novel least-squares formulation. The resulting method avoids the need for line integrals

and can be used to guarantee conservation and consistency (and, if desired, monotonicity) of the linear map.

The remapping problem is closely connected to conservative advection of scalar fields, using a technique known as semi-Lagrangian advection. This technique is employed by, for instance, the Conservative Semi-Lagrangian Multi-tracer Transport Scheme (CSLAM) (Lauritzen et al. 2010; Ullrich et al. 2013; Erath et al. 2013). By defining the source or target mesh as the location of Lagrangian fluid parcels at two different points in time, conservative remapping can be employed to define a conservative advection operator.

The outline of this paper is as follows. Section 2 describes the mathematical theory underlying linear remapping operators, and how conservation, consistency and monontonicity can be described in terms of the coefficients of the remapping matrix. One particular example of the construction of an arbitrarily high-order conservative and consistent (and possibly monotone) remapping operator is then pursued in section 3: Namely, the map that takes a discrete field from a nodal finite element mesh to a finite volume target mesh. The results of testing the resulting algorithm is then presented in section 4 followed by conclusions in section 5. The appendices provide a simple example of the construction of a linear map and provide additional details on the search algorithm for the overlap grid.

2. Mathematical Foundations

Consider some surface Ω, such as the unit sphere. Functions $\psi : \Omega \to \mathbb{R}$ are discretized by sampling ψ at discrete nodes, via pointwise sampling, or over discrete regions, via an area average. The finite set of discrete nodes or regions is then referred to as the *degrees of freedom* of a discretization. Note that this definition requires that degrees of freedom be associated with the values of ψ, and not with secondary information such as derivatives of ψ or the coefficients of

a spectral expansion (unless those coefficients also correspond to point values, such as the case of nodal finite element methods). Conserved quantities, such as mass, are represented via a local density variable stored at each degree of freedom. The complete set of all discrete density values is denoted by the vector $\boldsymbol{\psi}$. The operation of discretizing ψ to $\boldsymbol{\psi}$ is denoted by $\boldsymbol{\psi} = \mathbf{D}[\psi]$.

In the remapping problem, discretizations are defined for the source and target meshes. Let $\mathscr{F}_i^t$ denote the degrees of freedom on the target mesh, where $i \in [1, \ldots, f^t]$ and f^t is the total number of degrees of freedom. The set of all degrees of freedom is denoted $\mathscr{F}^t$. Each degree of freedom is then associated with a local weight J_i^t. For finite volumes the local weight J_i^t would represent the geometric area of the associated region. For nodal finite elements, the local weight J_i^t represents the value of the global Jacobian, or some global integral of the associated basis function. The local weights then induce an integration operator (or quadrature rule) denoted by $I^t[\cdot]$ and defined as

$$\int_\Omega \psi dA \approx I^t[\boldsymbol{\psi}^t] \equiv \sum_{i=1}^{f^t} \psi_i^t J_i^t, \tag{1}$$

where $\boldsymbol{\psi}^t$ denotes the discretization of ψ on the target mesh, with components ψ_i^t. On the unit sphere, one would expect that the degrees of freedom would have complete coverage of the surface, *i.e.* if $\mathbf{1}$ denotes the vector where every entry is 1 then

$$I^t[\mathbf{1}] = \sum_{i=1}^{f^t} J_i^t = 4\pi, \tag{2}$$

although this is not necessarily the case in practice. In particular, since integration over finite elements is governed by the truncation error of the underlying reconstruction, one may observe that (2) only holds approximately. Similar quantities are then defined for the source mesh: Let $\mathscr{F}_j^s$ denote the degrees of freedom on the source mesh, with $j \in [1, \ldots, f^s]$ and total count f^s, total set $\mathscr{F}^s$, associated weights J_j^s and integration operator $I^s[\boldsymbol{\psi}^s]$.

To remap fields from the source mesh to the target mesh, a remapping operator $\mathbf{R}$ is defined,

$$\boldsymbol{\psi}^t = \mathbf{R}\boldsymbol{\psi}^s, \tag{3}$$

where $\boldsymbol{\psi}^t$ and $\boldsymbol{\psi}^s$ are discretizations of ψ on the target and source mesh, respectively. Although the remapping operator can be specified arbitrarily, we are motivated to define a remapping operator that is somehow consistent with the geometry of the underlying problem. That is, we expect

$$\mathbf{D}^t[\psi] \approx \mathbf{R}\mathbf{D}^s[\psi], \tag{4}$$

where $\mathbf{D}^t$ and $\mathbf{D}^s$ denote the discretizations of ψ on the target and source mesh, respectively. Equivalence of (3) and (4) is not guaranteed since information is generally lost during a discretization operation. Three desirable properties of the remapping operator are now defined: namely, conservation, consistency and monotonicity. These properties are defined as follows.

Definition 1: A remapping operator $\mathbf{R}$ is *conservative* iff the global mass of any field is maintained across the remapping operation:

$$\mathbf{R} \text{ conservative} \quad \Longleftrightarrow \quad \forall\, \boldsymbol{\psi}^s, \quad I^s[\boldsymbol{\psi}^s] = I^t[\mathbf{R}\boldsymbol{\psi}^s]. \tag{5}$$

Definition 2: A remapping operator $\mathbf{R}$ is *consistent* iff the constant field is maintained across the remapping operation:

$$\mathbf{R} \text{ consistent} \quad \Longleftrightarrow \quad \mathbf{1}^t = \mathbf{R}\mathbf{1}^s. \tag{6}$$

Definition 3: A remapping operator $\mathbf{R}$ is *monotone* iff the remapping operation cannot introduce additional global extrema:

$$\mathbf{R} \text{ monotone} \quad \Longleftrightarrow \quad \forall\, \boldsymbol{\psi}^s \quad \forall\, i \in [1,\ldots,f^t] \quad \min \boldsymbol{\psi}^s \leq \psi_i^t \leq \max \boldsymbol{\psi}^s. \tag{7}$$

a. Linear remapping operators

This paper focuses on *linear remapping operators*. That is, where $\mathbf{R}$ can be written as a matrix-vector multiply operation,

$$\boldsymbol{\psi}^t = \mathbf{R}\boldsymbol{\psi}^s \quad \Longleftrightarrow \quad \psi_i^t = \sum_{j=1}^{f^s} R_{ij}\psi_j^s, \tag{8}$$

where R_{ij} denotes the coefficients of $\mathbf{R}$. In this context, the three properties described above have a clear meaning in terms of the coefficients of $\mathbf{R}$.

Proposition 1: The linear remapping operator $\mathbf{R}$ is *conservative* iff

$$\forall\ j \in [1,\ldots,f^s] \quad \sum_{i=1}^{f^t} R_{ij}J_i^t = J_j^s. \tag{9}$$

Proof: From (5) and the definition of the integration operator (1), conservation can be written as

$$\forall\ \boldsymbol{\psi}^s \qquad \sum_{j=1}^{f^s} \psi_j^s J_j^s = \sum_{i=1}^{f^t} \psi_i^t J_i^t. \tag{10}$$

Then using (8),

$$\sum_{j=1}^{f^s} \psi_j^s J_j^s = \sum_{i=1}^{f^t} J_i^t \sum_{j=1}^{f^s} R_{ij}\psi_j^s = \sum_{j=1}^{f^s} \psi_j^s \sum_{i=1}^{f^t} R_{ij}J_i^t. \tag{11}$$

However, since (11) must hold for all fields ψ_j^s, equivalence implies (9). ■

Proposition 2: The linear remapping operator $\mathbf{R}$ is *consistent* iff

$$\forall\ i \in [1,\ldots,f^t] \quad \sum_{j=1}^{f^s} R_{ij} = 1. \tag{12}$$

Proof: From (6) and (8),

$$\mathbf{1}^t = \mathbf{R}\mathbf{1}^s \quad \Longleftrightarrow \quad 1 = \sum_{j=1}^{f^s} R_{ij}. \quad \blacksquare \tag{13}$$

Proposition 3: The linear remapping operator $\mathbf{R}$ is *monotone* iff it is consistent and

$$\forall\ (i,j) \in [1,\ldots,f^t] \times [1,\ldots,f^s] \quad R_{ij} \geq 0. \tag{14}$$

Proof: Assume $\mathbf{R}$ is monotone. The field $\mathbf{1}^s$ satisfies $\min \mathbf{1}^s = \max \mathbf{1}^s = 1$ and so $\forall i$, $\psi^t = \mathbf{R}\psi^s \Longrightarrow$ $1 \leq \psi_i^t \leq 1$, which in turn implies $\psi^t = \mathbf{1}^t$ and so consistency is satisfied. To show $\forall (i,j)\ R_{ij} \geq 0$ assume $\exists (i,j)$ such that $R_{ij} < 0$. Let $\psi_j^s = 1$ and $\psi_k^s = 0\ \forall\ k \neq j$. Then

$$\psi_i^t = \sum_{k=1}^{f^s} R_{ik}\psi_k^s = R_{ij} < 0, \tag{15}$$

which contradicts (7).

Now assume $\mathbf{R}$ is consistent and satisfies (14). Then

$$\min_i \psi_i^t = \min_i \sum_{j=1}^{f^s} R_{ij}\psi_j^s \geq \min_j \psi_j^s \left(\sum_{j=1}^{f^s} R_{ij} \right) = \min_j \psi_j^s, \tag{16}$$

where the inequalities hold due to non-negativity of R_{ij} and the last equality holds due to consistency. The result is analogous for $\max_i \psi_i^t$. ■

Note that if $\mathbf{R}$ is conservative and consistent, it also follows that the source and target meshes must have the same area:

$$I^s[\mathbf{1}] = \sum_{j=1}^{f^s} J_j^s = \sum_{j=1}^{f^s}\sum_{i=1}^{f^t} R_{ij}J_i^t = \sum_{i=1}^{f^t} J_i^t \sum_{j=1}^{f^s} R_{ij} = \sum_{i=1}^{f^t} J_i^t = I^t[\mathbf{1}]. \tag{17}$$

This result further implies that for source and target meshes that do not have the same area it is impossible to define a linear remapping operator which is both conservative and consistent.

To clarify the mathematical notation used here, an example linear remapping operator is provided in Appendix A.

b. Local conservation

In order to introduce the concept of local conservation, one needs to first define some notion of geometric locality. Geometric regions associated with degrees of freedom $\mathscr{F}_i^t$ and $\mathscr{F}_j^s$ are denoted as Ω_i^t and Ω_j^s. The set of all geometric regions on the target and source meshes are denoted as $\mathbf{\Omega}^t$ and $\mathbf{\Omega}^s$. The *overlap region* associated with Ω_i^t and Ω_j^s is denoted by $\Omega_{i,j}^{ov} = \Omega_i^t \cap \Omega_j^s$ (see Figure 1). If $\Omega_{i,j}^{ov} \neq \varnothing$ then $\mathscr{F}_i^t$ and $\mathscr{F}_j^s$ are said to be *local*. The set of all overlap regions is referred to as the *overlap mesh* and denoted by $\mathbf{\Omega}^{ov}$ (note that the overlap mesh is sometimes referred to as the *supermesh* in the literature). Analogous to the source and target meshes, regions on the overlap mesh are associated with corresponding local weights $J_{i,j}^{ov}$, which must satisfy

$$J_j^s = \sum_{i=1}^{f^t} J_{i,j}^{ov}, \quad \text{and} \quad J_i^t = \sum_{j=1}^{f^s} J_{i,j}^{ov}. \tag{18}$$

The definition of Ω^s and Ω^t is sensitive to the choice of discretization (finite volume versus finite element), as follows.

- For finite volume discretizations, Ω is subdivided into regions that have a one-to-one correspondence with degrees of freedom by encoding the *volume average*. Hence, for finite volumes one can say that $\mathscr{F}_i^t$ and $\mathscr{F}_j^s$ are local if there is any geometric overlap between corresponding regions Ω_i^t and Ω_j^s.

- For nodal finite element discretizations, degrees of freedom are encoded as pointwise values, or equivalently as coefficients associated with a particular characteristic function (a modal characterization). An analogous definition of locality to finite volumes is obtained in terms of the support of the characteristic function associated with a particular degree of freedom; that is, Ω_j^s and Ω_i^t associated with particular degrees of freedom $\mathscr{F}_j^s$ and $\mathscr{F}_i^t$ are the geometric regions where the corresponding characteristic functions are non-zero, along with their closure.

Note that finite volumes specialize this definition under the imposition that each region has only one degree of freedom encoded via the constant characteristic function.

Local weights $J_{i,j}^{ov}$ may be calculated via integration over the overlap region,

$$J_{i,j}^{ov} = \int_{\Omega_{i,j}^{ov}} C_j^s(\mathbf{x}) C_i^t(\mathbf{x}), \tag{19}$$

where $C_j^s(\mathbf{x})$ and $C_i^t(\mathbf{x})$ are functions associated with the degrees of freedom $\mathscr{F}_j^s$ and $\mathscr{F}_i^t$ that satisfy

$$\int_\Omega C_j^s(\mathbf{x}) = J_j^s, \quad \int_\Omega C_i^t(\mathbf{x}) = J_i^t. \tag{20}$$

For a finite volume discretization C_j^s is equal to 1 within the associated region Ω_j^s (and analogously if discretized on the target mesh), whereas for a finite element discretization C_j^s is defined by the characteristic function associated with the degree of freedom (more on this in section 3a). Note that numerical errors may make exact computation of (19) difficult without the use of an advanced numerical integration technique, particularly in a manner that is consistent with (18). However, when mapping from a finite element mesh to a finite volume mesh this paper will only rely on knowing overlap areas $|\Omega_{i,j}^{ov}|$, which can be computed exactly.

The notion of locality then motivates the definition of a locally conservative operator:

Definition 4: The linear remapping operator $\mathbf{R}$ is *locally conservative* if it is conservative and

$$\Omega_{i,j}^{ov} = \varnothing \Longrightarrow R_{ij} = 0. \tag{21}$$

c. Local sub-maps

The notion of locality is particularly handy when constructing the remapping operators, since the global linear map $\mathbf{R}$ can be constructed using linear sub-maps $\hat{\mathbf{R}}$ that are only associated with a limited set of degrees of freedom from the source mesh. Local sub-maps further possess

analogues of conservation and consistency which are helpful for building global linear maps:

Definition 5: A linear sub-map operator $\hat{\mathbf{R}}$ is *conservative* in $A \subseteq [1,\ldots,f^s]$ if

$$j \in A \Rightarrow \sum_{i=1}^{f^t} \hat{R}_{ij} \left(\sum_{\ell \in A} J^{ov}_{i,\ell} \right) = J^s_j \quad \text{and} \quad j \notin A \Rightarrow \sum_{i=1}^{f^t} \hat{R}_{ij} \left(\sum_{\ell \in A} J^{ov}_{i,\ell} \right) = 0. \tag{22}$$

This definition could hold for any set of points A, but typically the set A consists of points that share a common geometric region Ω^s_i, such as in the case of a finite element discretization. For a finite volume discretization, source elements are usually considered in isolation and so the set A consists of only a single degree of freedom.

Definition 6: A linear sub-map operator $\hat{\mathbf{R}}$ is *consistent* in $B \subseteq [1,\ldots,f^t]$ if

$$i \in B \Rightarrow \sum_{j=1}^{f^s} \hat{R}_{ij} = 1 \quad \text{and} \quad i \notin B \Rightarrow \sum_{j=1}^{f^s} \hat{R}_{ij} = 0. \tag{23}$$

When constructing linear sub-maps, the set B is typically the set of degrees of freedom on the target mesh which are local to degrees of freedom A on the source mesh.

Definition 7: A set of linear sub-maps $\hat{\mathbf{R}}^{(1)},\ldots,\hat{\mathbf{R}}^{(N)}$ is *complete* if (i) $A^{(1)} \cup \cdots \cup A^{(N)} = [1,\ldots,f^s]$, (ii) $B^{(1)} \cup \cdots \cup B^{(N)} = [1,\ldots,f^t]$, (iii) $n \neq m$ implies $A^{(n)} \cap A^{(m)} = \varnothing$ (iv) $\hat{\mathbf{R}}^{(n)}$ is conservative in $A^{(n)}$ for $1 \leq n \leq N$, and (v) $\hat{\mathbf{R}}^{(m)}$ is consistent in $B^{(m)}$ for $1 \leq m \leq N$.

These definitions then motivate the following result, which is the fundamental theory for constructing global remapping operators as a combination of local sub-maps:

Theorem 1: Let $\hat{\mathbf{R}}^{(1)},\ldots,\hat{\mathbf{R}}^{(N)}$ be a complete set of linear sub-maps which are conservative in $A^{(1)},\ldots,A^{(N)}$. Then the global linear map constructed via

$$R_{ij} = \frac{1}{J_i^t}\sum_{k=1}^{N}\hat{R}_{ij}^{(k)}\left(\sum_{\ell\in A^{(k)}} J_{i,\ell}^{ov}\right) \tag{24}$$

is conservative and consistent.

Proof: To show consistency we use property (i), (ii) and (v) (Definition 7) and (23):

$$\begin{aligned}
\sum_{j=1}^{f^s} R_{ij} &= \frac{1}{J_i^t}\sum_{j=1}^{f^s}\sum_{k=1}^{N}\hat{R}_{ij}^{(k)}\left(\sum_{\ell\in A^{(k)}} J_{i,\ell}^{ov}\right) \\
&= \sum_{k=1}^{N}\frac{1}{J_i^t}\left(\sum_{\ell\in A^{(k)}} J_{i,\ell}^{ov}\right)\sum_{j=1}^{f^s}\hat{R}_{ij}^{(k)} \\
&= \sum_{k=1}^{N}\frac{1}{J_i^t}\left(\sum_{\ell\in A^{(k)}} J_{i,\ell}^{ov}\right)\delta_i^{B^{(k)}} && (\hat{\mathbf{R}}^{(k)} \text{ consistent in } B^{(k)}) \\
&= 1 && \text{(property (i) and (ii)).}
\end{aligned}$$

Here $\delta_i^{B^{(k)}}$ is an indicator that is 1 if $i \in B^{(k)}$ and 0 otherwise.

Conservation follows almost immediately from property (ii), (iii) and (v) (Definition 7) and (22), which collectively imply that only one linear sub-map will have a non-zero weighted column sum:

$$\sum_{i=1}^{f^t} R_{ij}J_i^t = \sum_{k=1}^{N}\sum_{i=1}^{f^t}\hat{R}_{ij}^{(k)}\left(\sum_{\ell\in A^{(k)}} J_{i,\ell}^{ov}\right) = J_j^s. \qquad \blacksquare$$

Note that if the linear sub-map is monotone then the global composition will inherit some notion of local monotonicity. Local monotonicity is even stronger than the global monotonicity described in Definition 3, in that the global map will not introduce additional local extrema.

3. Remapping Finite Elements to Finite Volumes

A global mapping operator from finite elements to finite volumes is now developed using the theory of section 2. Consistent with the notion of degrees of freedom representing the values of

ψ, this paper focuses specifically on nodal finite element methods over the set of Gauss-Lobatto-Legendre (GLL) nodes. The set of degrees of freedom on the source mesh are defined at the N_p^2 GLL nodes within the reference element (see Figure 2). The operator is first developed for discontinuous finite elements (*i.e.* admitting co-located degrees of freedom between adjacent elements); if continuous finite elements are used, as in the case of the spectral element method, the rows of the discontinuous remapping operator can be combined via direct stiffness summation (Deville et al. 2002) without affecting conservation, consistency or monotonicity of the operator. As a consequence of (17), a conservative map from finite elements to finite volumes only exists if the degrees of freedom of the source (finite element) mesh satisfy some notion of geometric consistency:

Definition 8: A finite element on the source mesh with region Ω_j^s and degrees of freedom $A \subseteq [1,\ldots,f^s]$ is *geometrically consistent* if

$$|\Omega_j^s| = \sum_{k\in A} J_k^s. \tag{25}$$

This definition implies that the geometric area of the finite element mesh must be exactly distributed over all degrees of freedom. Following on this definition, it is guaranteed that there exists at least one conservative, consistent and monotone linear sub-map:

Theorem 2: There exists at least one consistent, conservative, monotone linear sub-map from a geometrically consistent GLL finite element of order N_p to the target mesh.

Proof: By construction. Consider a single GLL element with N_p^2 nodal degrees of freedom, taken from a subset of all degrees of freedom on the source mesh via the indexing function $\sigma : (p,q) \rightarrow [1,\ldots,f^s]$ with $(p,q) \in [0,\ldots,N_p-1]^2$ and $(p_1,q_1) \neq (p_2,q_2) \Rightarrow \sigma(p_1,q_1) \neq \sigma(p_2,q_2)$. A linear

sub-map is defined by a weighted average over all GLL nodes:

$$\hat{R}^0_{ij} = \begin{cases} J^s_j \left[\sum_{p=0}^{N_p-1} \sum_{q=0}^{N_p-1} J^s_{\sigma(p,q)} \right]^{-1}, & \text{if } \exists\ (p,q) \text{ such that } \sigma(p,q) = j \text{ and } \Omega^{ov}_{i,j} \neq \varnothing, \\ 0 & \text{otherwise.} \end{cases} \tag{26}$$

Consistency over $B = \{i : \mathscr{F}^t_i \cap \mathscr{F}^s_j \text{ local}\}$ is easily demonstrated from (23). Conservation over $A = \{\sigma(p,q) : (p,q) \in [0,\ldots,N_p-1]^2\}$ follows by observing $\hat{R}^0_{ij} = 0$ for $j \notin A$ and

$$\sum_{\ell \in A} J^{ov}_{i,\ell} = |\Omega^s_j|, \tag{27}$$

which in turn implies

$$\sum_{i=1}^{f^t} \hat{R}^0_{ij} \left(\sum_{\ell \in A} J^{ov}_{i,\ell} \right) = J^s_j \left[\sum_{p=0}^{N_p-1} \sum_{q=0}^{N_p-1} J^s_{\sigma(p,q)} \right]^{-1} |\Omega^s_j| = J^s_j. \tag{28}$$

Monotonicity follows since $\hat{R}^0_{ij}$ is consistent and all entries of $\hat{R}^0_{ij}$ are non-negative. ■

Although the linear sub-map $\hat{\mathbf{R}}^0$ satisfies conservation, consistency and monotonicity, it is undesirable as a linear remapping operator since it "averages out" the sub-grid-scale variation associated with the finite element discretization. Consequently the remainder of this section will focus on constructing an improved linear sub-map operator. To this end, the following basic algorithm is followed:

```
Given SourceMesh and TargetMesh calculate OverlapMesh
```

```
For each source region fi in SourceMesh
  Compute a "first guess" conservative and consistent linear sub-map
    from fi to the OverlapMesh
  Project the "first guess" map onto the space of exactly conservative
    and consistent linear sub-maps
  If monotonicity is required, adjust coefficients accordingly
  Compose the linear sub-map in the global remapping operator R
Store global remapping operator R
```

The generation of the overlap mesh follows the algorithm described in Appendix B. Since the global map is simply a composition of sub-maps which are defined over source elements on the finite element mesh, the remainder of this section will simply focus on construction of sub-maps with the desired properties.

a. Choice of basis functions

Construction of an approximately conservative map relies on the use of *basis functions* to provide a continuous analogue to the nodal discretization. Two requirements are imposed on these functions: First, the basis functions must also be characteristic functions – that is, at each GLL node exactly one basis function must take the value 1 and all other basis functions must have value 0. Second, for sake of consistency, the basis functions must be a partition of unity over the finite element. Besides these two requirements, the choice of basis is at the discretion of the user.

For quadrilateral elements we choose basis functions defined via a tensor product, wherein N_p 1D basis functions $C_m(x)$ ($m = 0, \ldots, N_p - 1$) are cross-multiplied to yield N_p^2 2D basis functions

and a corresponding reconstruction,

$$\psi_j^s(\mathbf{x}) = \sum_{m=0}^{N_p-1}\sum_{n=0}^{N_p-1} (\psi_j^s)_{(m,n)} C_m(\alpha(\mathbf{x}))C_n(\beta(\mathbf{x})), \tag{29}$$

The coordinates $\alpha(\mathbf{x}_k)$ and $\beta(\mathbf{x}_k)$ are defined implicitly via the coordinate transform of Guba et al. (2014). For a quadrilateral region on the source mesh with corner points $\mathbf{x}_k$ ($k = 1,\ldots,4$) arranged in counter-clockwise order,

$$\begin{aligned}
\hat{\mathbf{x}}(\alpha,\beta) &= \mathbf{x}_1(1-\alpha)(1-\beta) + \mathbf{x}_2(1+\alpha)(1-\beta) + \mathbf{x}_3(1+\alpha)(1+\beta) + \mathbf{x}_4(1-\alpha)(1+\beta), \\
\mathbf{x}(\alpha,\beta) &= \frac{\hat{\mathbf{x}}(\alpha,\beta)}{\|\hat{\mathbf{x}}(\alpha,\beta)\|}.
\end{aligned} \tag{30}$$

Choosing basis functions which are polynomials of maximum degree (the cardinal functions over GLL points and the standard nodal finite element basis) leads to a non-monotone remapping operator of the highest formal order-of-accuracy; whereas choosing a set of basis functions with the limited range $[0,1]$ leads to a low-order, but monotone, operator. Approximate conservation is enforced by choosing a basis whose global integral equals its associated nodal weight. Consistency follows as long as the set of all basis functions is a partition of unity. Herein two choices of basis functions are made:

(i) Non-monotone basis: Our non-monotone basis over GLL elements is given by the cardinal functions over GLL nodes (Boyd 2001, Appendix F). In terms of the Legendre polynomials of order $N_p - 1$, denoted $P_{N_p-1}(x)$, these are

$$C_m(x) \equiv \frac{(x^2-1)}{N_p(N_p-1)P_{N_p-1}(x_j)(x-x_j)} \frac{dP_{N_p-1}(x)}{dx}, \tag{31}$$

with corresponding weights

$$w_m \equiv \int_{-1}^{1} C_m(x)dx = \frac{2}{N_p(N_p-1)\left[P_{N_p-1}(x_j)\right]^2}. \tag{32}$$

The cardinal functions are plotted in Figure 3 (a,c) for $N_p = 3,4$. For 2D GLL finite elements, these cardinal functions and weights are written via tensor product,

$$C_{m,n}(x,y) = C_m(x)C_n(y), \qquad w_{m,n} = w_m w_n. \tag{33}$$

Given some local notion of area $J(\mathbf{x})$ (such as the Jacobian associated with a coordinate transform), the local weight J_j^s at the GLL point $\mathbf{x}_{m,n}$ is typically approximated as the product $J(\mathbf{x}_{m,n})w_{m,n}$. However, since this notion of J_j^s is not geometrically consistent, we instead suggest a closely related, but modified definition $J_j^s = |\Omega_j^s| w_{m,n}$.

(ii) Monotone basis: The monotone basis uses a set of monotonized cardinal functions $\hat{C}_m(x)$ which resemble the standard non-monotone cardinal functions (31) under the further constraint $0 \leq \hat{C}_m(x) \leq 1$. However, to enforce conservation we further require

$$\int_{-1}^{1} \hat{C}_m(x)dx = w_m. \tag{34}$$

For $N_p = 2$, $\hat{C}_m = C_m$ actually satisfies these criteria. However, for larger values of N_p it is the case that $C_j(x) < 0$ over some interval, and so the standard cardinal functions do not satisfy the desired monotone property. Consequently a new set of basis functions are constructed which satisfy consistency and conservation but with the limited range $[0,1]$. For $N_p = 3$ there is a unique solution for piecewise quadratic polynomials given by

$$\begin{aligned} N_p = 3: \qquad \hat{C}_0(x) &= \begin{cases} \frac{1}{2}(x^2 - x) & x < 0, \\ 0 & x \geq 0, \end{cases} \\ \hat{C}_1(x) &= 1 - x^2, \\ \hat{C}_2(x) &= \hat{C}_0(-x). \end{aligned} \tag{35}$$

For $N_p = 4$ there is no solution with piecewise quadratic polynomials. Piecewise cubic polynomials admit one free parameter, which we arbitrarily choose so that the reconstruction is C^1

continuous. This choice yields the solution

$$
\begin{aligned}
N_p = 4: \qquad \hat{C}_0(x) &= \begin{cases} \frac{1}{16}\left\{\left[(1+\sqrt{5})+(5+\sqrt{5})x\right](1-5x^2)\right\} & x < -1/\sqrt{5}, \\ 0 & x \geq -1/\sqrt{5} \end{cases} \\
\hat{C}_1(x) &= \begin{cases} 1-\hat{C}_0(x), & x < -1/\sqrt{5}, \\ \frac{1}{4}\left(2-3\sqrt{5}x+5\sqrt{5}x^3\right), & -1/\sqrt{5} \leq x \leq 1/\sqrt{5}, \\ 0 & x \geq 1/\sqrt{5} \end{cases} \\
\hat{C}_2(x) &= \hat{C}_1(-x), \\
\hat{C}_3(x) &= \hat{C}_0(-x).
\end{aligned} \tag{36}
$$

Monotonized cardinal functions can be similarly specified for $N_p > 4$. These functions are plotted in Figure 3 (b,d) for $N_p = 3, 4$.

One curious result emerges from this construction: Although for $N_p = 2$ the monotone basis can correctly capture linear variation over a finite element, for $N_p > 2$ all monotone basis functions have zero derivative at interior GLL nodes, and consequently cannot represent linear variations within the element. This suggests that smoothly varying fields may be more poorly captured when construction a monotone map with $N_p > 2$ (as we shall see later). The choice of a monotone basis that avoids this problem is confounded by the need for conservation, automatically eliminating the second-order bilinear interpolant as an option.

b. Building a "first guess" sub-map

The "first guess" sub-map required by this algorithm only needs to satisfy the conservation and consistency property approximately. Here it is constructed by using high-order triangular quadrature to integrate each characteristic function over all polygonal regions on the overlap mesh via polygonal subdivision (see Figure 4). The triangular quadrature rules employed by this package

are given by Dunavant (1985), and depicted in Figure 5 for triangular quadrature rules of order 1, 4 and 8. The triangular quadrature rule should at least match the order of accuracy of the finite element method to ensure the map exhibits the correct order-of-accuracy. Only triangular quadrature rules with nonnegative weights are considered, since the use of negative weights could lead to a loss of monotonicity. Given a triangular region with corner points $(\mathbf{x}_{i,j}^{ov})_k$ ($k \in \{1,2,3\}$) connected via great circle arcs, the quadrature rule $(\hat{w}_k, \hat{\alpha}_k, \hat{\beta}_k, \hat{\gamma}_k)$ is applied via

$$\int_{\mathscr{F}_{i,j}^{ov}} \psi_j^s(\mathbf{x}) dA \approx \sum_{k=1}^{N_q} \psi_j^s(\mathbf{x}_k) \hat{w}_k J_{i,j}^{ov}, \tag{37}$$

$$\text{with} \quad \mathbf{x}_k = (\mathbf{x}_{i,j}^{ov})_1 \hat{\alpha}_k + (\mathbf{x}_{i,j}^{ov})_2 \hat{\beta}_k + (\mathbf{x}_{i,j}^{ov})_3 (1 - \hat{\alpha}_k - \hat{\beta}_k),$$

where $\psi_j^s(\mathbf{x}_k)$ is defined in (29). This procedure yields a sub-map which is consistent as long as the basis functions are a partition of unity, but non-conservative since inexact quadrature is employed.

c. Consistency and Conservation Enforcement

Since conservation is not guaranteed by the above procedure, we now enforce conservation by orthogonal projection of the sub-map onto the space of conservative and consistent maps. In some sense, this projected solution is optimal since the projected map is closest (in the sense of Euclidian distance) to the "first guess" map. The projection operation is performed by solving a least squares problem for all coefficients in the sub-map. This highlights a key strength of dividing the global map into sub-maps; namely enforcement of global conservation and consistency requires the solution of a large number of small, inexpensive optimization problems (one for each sub-map), rather than one very expensive global optimization problem.

Given an arbitrary linear sub-map $\hat{R}_{ij}^*$ with $\hat{f}^s = |A|$ source elements and $\hat{f}^t = |B|$ target elements, the corresponding conservative and consistent remapping operator $\hat{R}_{ij}$ is obtained as follows:

$$\text{Minimize} \quad \sum_{i=1}^{\hat{f}^t} \sum_{j=1}^{\hat{f}^s} \frac{1}{2} (\hat{R}_{ij} - \hat{R}_{ij}^*)^2 \quad \text{subject to conservation (22) and consistency (23).} \tag{38}$$

The least squares problem is solved directly via the Lagrangian. Vectors $\boldsymbol{\lambda}$ and $\boldsymbol{\kappa}$ are defined with elements λ_i, $i \in [1,\ldots,\hat{f}^t]$, and κ_j, $j \in [1,\ldots,\hat{f}^s-1]$ respectively. Note that the result (17) implies that the consistency and conservation conditions are linearly dependent, and so conservation is only imposed for the first $\hat{f}^s-1$ elements. The Lagrangian takes the form

$$\mathscr{L}(\mathbf{R},\boldsymbol{\lambda},\boldsymbol{\kappa}) = \sum_{i=1}^{\hat{f}^t}\sum_{j=1}^{\hat{f}^s}\frac{1}{2}(\hat{R}_{ij}-\hat{R}^*_{ij})^2 - \underbrace{\sum_{i=1}^{\hat{f}^t}\lambda_i\left[\left(\sum_{j=1}^{\hat{f}^s}\hat{R}_{ij}\right)-1\right]}_{\text{consistency}} - \underbrace{\sum_{j=1}^{\hat{f}^s-1}\kappa_j\left[\left(\sum_{i=1}^{\hat{f}^t}\hat{R}_{ij}J^t_i\right)-J^s_j\right]}_{\text{conservation}}. \quad (39)$$

The unique minimizer of the Lagrangian is then obtained by differentiating with respect to all coefficients $\hat{R}_{ij}$, λ_i and κ_j and leads to the linear system

$$\begin{pmatrix} \mathbf{I} & \mathbf{C}^T \\ \mathbf{C} & \mathbf{0} \end{pmatrix}\begin{pmatrix} \hat{\mathbf{R}}_{ij} \\ \boldsymbol{\lambda} \\ \boldsymbol{\kappa} \end{pmatrix} = \begin{pmatrix} \hat{\mathbf{R}}^*_{ij} \\ -\mathbf{1} \\ -\mathbf{J}^s \end{pmatrix}, \quad (40)$$

where $\mathbf{C}$ is the $(\hat{f}^t+\hat{f}^s-1)\times\hat{f}^t\hat{f}^s$ matrix defined by the derivatives $\partial\mathscr{L}/\partial\boldsymbol{\lambda}$ and $\partial\mathscr{L}/\partial\boldsymbol{\kappa}$. This system can be solved efficiently via Schur complement,

$$\hat{R}_{ij} = \hat{R}^*_{ij} - \mathbf{C}^T(\mathbf{C}\mathbf{C}^T)^{-1}\left[\mathbf{C}\hat{R}^*_{ij} + \begin{pmatrix} \mathbf{1} \\ \boldsymbol{J}^s \end{pmatrix}\right]. \quad (41)$$

Note that to further improve the efficiency of this calculation, the matrix $\mathbf{C}\mathbf{C}^T$ can be specified directly. If we define

$$S^2 = \sum_{i=1}^{\hat{f}^t}(J^t_i)^2, \quad (42)$$

then

$$\mathbf{C}\mathbf{C}^T = \begin{pmatrix} \hat{f}^s & & 0 & J_1^t & \cdots & J_1^t \\ & \ddots & & \vdots & & \vdots \\ 0 & & \hat{f}^s & J_{\hat{f}^t}^t & \cdots & J_{\hat{f}^t}^t \\ J_1^t & \cdots & J_{\hat{f}^t}^t & S^2 & & 0 \\ \vdots & & \vdots & & \ddots & \\ J_1^t & \cdots & J_{\hat{f}^t}^t & 0 & & S^2 \end{pmatrix} \begin{matrix} \\ \\ \hat{f}^t \text{ entries} \\ \\ \\ (\hat{f}^s - 1) \text{ entries} \end{matrix} . \tag{43}$$

d. A note about convergence

An advantage of using the least squares procedure is that it does not affect the accuracy (in the sense of convergence) of the "first guess" map, in accordance with the following theorem.

Theorem 3: If $\hat{\mathbf{R}}^*$ is constructed using the non-monotone reconstruction in (31) with a triangular quadrature rule of at least order N_p, then $\psi^t = \hat{\mathbf{R}}\mathbf{D}^s[\psi]$ is convergent with order N_p.

Sketch of Proof: For a sufficiently smooth field ψ define the exact map via

$$\hat{\mathbf{R}}_{exact}\mathbf{D}^s[\psi] = \mathbf{D}^t[\psi]. \tag{44}$$

By construction, $\hat{\mathbf{R}}_{exact}$ must be conservative and consistent. Note that since order N_p quadrature is used for constructing $\hat{\mathbf{R}}^*$, ψ^t will converge to $\mathbf{D}^t[\psi]$ with order $O(\Delta x^{N_p})$. However, since (38) represents the closest sub-map (in the sense of Eulerian distance) to $\hat{\mathbf{R}}^*$ that is conservative and consistent, then

$$\|\hat{\mathbf{R}} - \hat{\mathbf{R}}^*\|_2 < \|\hat{\mathbf{R}}_{exact} - \hat{\mathbf{R}}^*\|_2 = O(\Delta x^{N_p}), \tag{45}$$

and so $\hat{\mathbf{R}}$ is also convergent with order N_p. ■

e. Monotonicity Preservation

In order to impose monotonicity, the least squares problem (38) can be augmented with an additional boundedness condition given by (14). Solving the resulting constrained and bounded least-squares problem can then be done via an interior point method (see, for example, Boyd and Vandenberghe (2009)). However, this additional criteria can be computationally taxing, and so another approach is used in practice. After computing the unique conservative and consistent sub-map from (38) using the procedure described above, the resulting linear sub-map may contain small negative values which need to be removed. To do so, the following theorem is used:

Theorem 4: If $\hat{R}_{ij}^{(1)}$ and $\hat{R}_{ij}^{(2)}$ are conservative and consistent linear sub-maps over $A^{(1)} = A^{(2)}$ and $B^{(1)} = B^{(2)}$ respectively, then for $\omega \in [0,1]$, $\hat{R}_{ij} = \omega\hat{R}_{ij}^{(1)} + (1-\omega)\hat{R}_{ij}^{(2)}$ is a consistent and conservative linear sub-map.

Proof: By linearity of (22) and (23). ■

Consequently, if $\hat{R}_{ij}^{s}$ is the conservative and consistent linear sub-map obtained from the least squares procedure then the linear sub-map constructed via

$$\hat{R}_{ij} = \omega\hat{R}_{ij}^{0} + (1-\omega)\hat{R}_{ij}^{s} \tag{46}$$

is also conservative and consistent. Monotonization of $\hat{R}_{ij}^{s}$ then simply relies on finding a value of ω sufficiently large that $\hat{R}_{ij}$ has no negative entries. In fact, the choice

$$\omega = \max_{i,j}\left[\max\left(\frac{-\hat{R}_{ij}^{s}}{|\hat{R}_{ij}^{0} - \hat{R}_{ij}^{s}|}, 0\right)\right]. \tag{47}$$

meets this criterion and so is used to define a monotone sub-map.

4. Numerical Results

The meshes used for validation of the linear maps are plotted in Figure 6, although only meshes (a)-(c) will be used for the idealized study. These include (a) an equiangular cubed-sphere mesh, (b) a great circle latitude-longitude mesh and (c) a geodesic mesh. The great circle latitude-longitude mesh is constructed analogous to a regular latitude-longitude mesh, but all edges are approximated as great circle arcs (note that in a regular latitude-longitude mesh lines of constant latitude are not great circle arcs). This approximation has the greatest deviation from the regular latitude-longitude mesh in the polar region (Ullrich et al. 2009). The geodesic mesh is constructed by taking the dual of an icosahedral mesh, which is in turn obtained by subdividing the triangular faces of an icosahedron into sub-triangles. The resulting mesh is composed largely of hexagons, with exactly 12 pentagons appearing due to the icosahedral corner nodes.

The analysis mirrors the approach of Lauritzen and Nair (2007): We consider three idealized test cases of varied complexity to understand the error measures produced by the linear maps from GLL elements to finite volumes. The three analytical fields studied are depicted in Figure 7. Following Jones (1999) and Lauritzen and Nair (2007) the first field is a relatively smooth function resembling a spherical harmonic of order 2 and azimuthal wavenumber 2, given by

$$\psi = 2 + \cos^2\theta \cos(2\lambda), \qquad (Y_2^2). \tag{48}$$

The second field is a relatively high frequency wave similar to a spherical harmonic of order 32 and azimuthal wavenumber 16, given by

$$\psi = 2 + \sin^{16}(2\theta)\cos(16\lambda), \qquad (Y_{32}^{16}). \tag{49}$$

These fields are used to test performance for a smooth well-resolved field and a high-frequency poorly resolved field with rapidly changing gradients. The third field is a dual stationary vortex

(Nair and Machenhauer 2002). The field is given by

$$\psi = 1 - \tanh\left[\frac{\rho'}{d}\sin(\lambda' - \omega' t)\right], \qquad \text{(Vortex)} \tag{50}$$

where the radius $\rho' = r_0 \cos\theta'$, with angular velocity

$$\omega'(\theta') = \begin{cases} 0 & \text{if } \rho' = 0, \\ \frac{V_t}{\rho'} & \text{if } \rho' \neq 0, \end{cases} \tag{51}$$

and normalized tangental velocity

$$V_t = \frac{3\sqrt{3}}{2}\mathrm{sech}^2\rho' \tanh\rho'. \tag{52}$$

The (λ', θ') refer to a rotated spherical coordinate system with a pole located at (λ_0, θ_0). Following Lauritzen and Nair (2007) we choose $(\lambda_0, \theta_0) = (0, 0.6)$, $r_0 = 3$, $d = 5$ and $t = 6$.

Standard error measures are employed:

$$L_1 \equiv \frac{I^t\left[\left|\mathbf{RD}^s[\psi] - \mathbf{D}^t[\psi]\right|\right]}{I^t\left[\left|\mathbf{D}^t[\psi]\right|\right]}, \qquad L_2 \equiv \frac{\sqrt{I^t\left[\left|\mathbf{RD}^s[\psi] - \mathbf{D}^t[\psi]\right|^2\right]}}{\sqrt{I\left[\left|\mathbf{D}^t[\psi]\right|^2\right]}}, \tag{53}$$

$$L_\infty \equiv \frac{\max\left|\mathbf{RD}^s[\psi] - \mathbf{D}^t[\psi]\right|}{\max\left|\mathbf{D}^t[\psi]\right|}, \tag{54}$$

$$L_{min} \equiv \frac{\min\left(\mathbf{D}^t[\psi]\right) - \min\left(\mathbf{RD}^s[\psi]\right)}{\max\left|\mathbf{D}^t[\psi]\right|}, \qquad L_{max} \equiv \frac{\max\left(\mathbf{RD}^s[\psi]\right) - \max\left(\mathbf{D}^t[\psi]\right)}{\max\left|\mathbf{D}^t[\psi]\right|} \tag{55}$$

In some general sense, the error measures L_1 identifies errors in large-scale features, L_2 identifies errors in small-scale features and L_∞ identifies the largest pointwise error. The error measures L_{min} and L_{max} identify undershoots and overshoots, respectively, by taking on positive values when the global extreme values are enhanced.

In the following sections the source discretization $\mathbf{D}^s[\psi]$ is generated by sampling ψ at each nodal GLL point on the source mesh. The results of the remapping operation are compared to a

target discretization $\mathbf{D}^t[\psi]$ generated via 8^{th} order triangular quadrature over each polygon on the target mesh. The default configuration further use a 4^{th}-order triangular quadrature rule is used to construct the "first guess" map.

a. Cubed-sphere mesh to great circle latitude-longitude mesh (non-monotonic)

Figure 8 shows standard error measures for the conservative and consistent linear map from the cubed-sphere grid with $n_e \times n_e$ elements per panel ($n_e = 15, 30, 60$) to the great circle latitude-longitude grid with 1° grid spacing (consisting of 360 longitudinal elements and 180 latitudinal elements). The number of GLL nodes per element (and hence the order of accuracy of the linear map) is given by $N_p = 2, 3$ or 4. All results are conservative to machine truncation (not shown). Error measures are smallest for the smooth Y_2^2 field, as expected. All fields further show progressively decreasing error norms with increasing n_e and N_p. Further, the Y_{32}^{16} and Vortex meshes show convergence rates which closely match $O(n_e^{-N_p})$. The convergence rate for the Y_2^2 field is almost $O(n_e^{-N_p})$, except for the fourth-order scheme which is not quite fourth-order convergent at the finest resolution. The loss of perfect convergence is due to insufficient resolution on the target grid, which affects both the construction of the "first guess" map and the evaluation of the reference solution.

Figure 9 shows L_{min} and L_{max} for the mapping problem above. In general there is a consistent decrease in the errors of the extreme values of each field, although these results are far less consistent than the results for the L_p norms. Overshoots and undershoots are observed in many of the simulations with $N_p > 2$ and are identified by circled data points.

b. Cubed-sphere mesh to great circle latitude-longitude mesh (monotonic)

Figure 10 provides error norms for the cubed-sphere to great circle latitude-longitude grid mapping described above, except here with strict monotonicity enforced on the linear map via the procedure described in section 3e. The error norms are significantly worse, compounded by the fact that any monotone method is limited to at most second-order convergence. As expected (following the discussion in section 3a), the $N_p > 2$ results are actually worse than the $N_p = 2$ results for the Y_2^2 field. Figure 11 shows L_{min} and L_{max} for the conservative, consistent and monotone map. These error norms are always negative, which confirms that the global minimum and maximum are not enhanced by the linear map.

c. Cubed-sphere mesh to geodesic mesh (non-monotonic)

To verify robustness of the algorithm, remapping has also been performed from the cubed-sphere grid to the $N_i = 72$ geodesic mesh (generated from N_i triangular elements along each face of the icosahedron). Standard error measures are plotted in Figure 12 along with L_{min} / L_{max} in Figure 13. The error norms show generally consistent behavior as with the previous study, suggesting that the results are largely independent of the target mesh.

d. Refined cubed-sphere mesh to great circle latitude-longitude mesh (real data)

To test if the algorithm performs well in practice, the software is tested for remeshing of data from a variable-resolution cubed-sphere mesh (Figure 6d) to the great circle latitude-longitude grid (Figure 6b). The variable resolution mesh has been designed for a study of California climatology, and so provides an enhancement to 0.25° resolution over California from 1° global resolution. Integration has been performed using the Community Earth System Model spectral element dynamical core (Neale et al. 2010) using the variable resolution capability described in

Zarzycki et al. (2014). The result of the remapping algorithm is plotted in Figure 14, showing a relatively smooth field (surface pressure) and a highly discontinuous field where monotonicity preservation is necessary (percentage plant functional type). Overall the algorithm performs well, with no obvious grid imprinting apparent on the result.

5. Conclusions

A mathematical theory underlying for conservative and consistent (and optionally monotone) linear maps between meshes on the sphere has been presented. To demonstrate the applicability of this theory, an algorithm has been developed for constructing arbitrary-order conservative and consistent linear maps between finite-element and finite-volume meshes. This method was then tested using a cubed-sphere source mesh and a great circle latitude-longitude target mesh or geodesic target mesh. The resulting remap scheme has been demonstrated to have the correct convergence rate for polynomials up to cubic degree (fourth-order), although there is no fundamental limit on the order of the scheme. A technique for constructing conservative, consistent and monotone maps was also discussed and led to second-order convergent linear maps. Testing was also performed on real data and the results observed to be satisfactory for real applications.

This algorithm has been extended for generating linear maps from finite-volumes to finite-volumes and/or finite-elements, which will be the topic of a future manuscript. It is also anticipated that the search algorithm and quadrature rule will be extended to support grid lines of constant latitude. This work will be used as a basis for constructing a semi-Lagrangian advection scheme on the sphere which provides high-order accuracy on arbitrary meshes.

a. Software availability

The software described in this manuscript has been released as part of the Tempest software package, and is available for use under the Lesser GNU Public License (LGPL). All software can be obtained from GitHub via the following clone URL:

`https://github.com/paullric/tempestremap.git`

b. Acknowledgements

The authors would like to thank Iulian Grindeanu and Vijay S. Mahadevan for several helpful discussions on the development of the search algorithm. The authors would like to further thank Hans Johansen and Dharshi Devendran for their discussions on the development of the remapping algorithm. We would also like to thank the input of the three anonymous reviewers for improving the clarity of the manuscript. This project is funded through the Department of Energy, Office of Science, Division for Advanced Scientific Computing Research and the "Multiscale Methods for Accurate, Efficient, and Scale-Aware Models of the Earth System" program.

APPENDIX A

An Example Linear Map

This appendix provides a simple 1D example of a finite element to finite volume linear map. Consider the 1D interval $\Omega = [0,1]$ covered by one finite element with $N_p = 4$ and divided into three finite volumes of equal width. The regions on the finite element mesh are regions of support for the non-monotone basis functions,

$$\Omega_1^s = \Omega_2^s = \Omega_3^s = \Omega_4^s = [0,1], \tag{A1}$$

and on the finite volume mesh are regions of equal width,

$$\Omega_1^t = \left[0, \tfrac{1}{3}\right], \quad \Omega_2^t = \left[\tfrac{1}{3}, \tfrac{2}{3}\right], \quad \Omega_3^t = \left[\tfrac{2}{3}, 1\right]. \tag{A2}$$

Degrees of freedom on the finite element mesh are stored at nodal points

$$x_1^s = 0, \quad x_2^s = \tfrac{1}{2} - \tfrac{1}{10}\sqrt{5}, \quad x_3^s = \tfrac{1}{2} + \tfrac{1}{10}\sqrt{5}, \quad x_4^s = 1. \tag{A3}$$

Local weights on the source mesh are given by (32),

$$J_1^s = \tfrac{1}{12}, \quad J_2^s = \tfrac{5}{12}, \quad J_3^s = \tfrac{5}{12}, \quad J_4^s = \tfrac{1}{12}, \tag{A4}$$

and on the target mesh by the geometric area,

$$J_1^t = J_2^t = J_3^t = \tfrac{1}{3}. \tag{A5}$$

Observe that these local weights satisfy (17) and geometric consistency (Definition 8), for $A = [1,2,3,4]$. By using exact integration over the characteristic functions on this finite element we can then obtain a linear mapping operator,

$$\mathbf{R} = \begin{pmatrix} \frac{35}{108} & \frac{35}{108} + \frac{5}{27}\sqrt{5} & \frac{35}{108} - \frac{5}{27}\sqrt{5} & \frac{3}{108} \\ -\frac{11}{108} & \frac{65}{108} & \frac{65}{108} & -\frac{11}{108} \\ \frac{3}{108} & \frac{35}{108} - \frac{5}{27}\sqrt{5} & \frac{35}{108} + \frac{5}{27}\sqrt{5} & \frac{35}{108} \end{pmatrix}. \tag{A6}$$

Note that since exact integration is used, this operator is already conservative and consistent and so is unaffected by the least squares procedure (section 3.c). The operator is not monotone, as is apparent from negative entries $R_{1,3}$, $R_{2,1}$, $R_{2,4}$ and $R_{3,2}$. If an inexact integration procedure were used, the least squares projection could be necessary to enforce conservation.

APPENDIX B

Overlap Mesh Generation Algortihm

This appendix provides an outline of the algorithm used for generating the overlap mesh. For serial overlap mesh generation this approach is far from optimal, but is potentially easier to parallelize than other methods, such as the advancing front method described in Farrell and Maddison (2011). Improved overlap mesh generation remains a topic for future work. The main function simply loops through all faces on the first mesh, first generating a path around the boundary of each face which accounts for intersections with the second mesh, and then follows the path to generate all faces contained within the path. The pseudocode for this algorithm is as follows:

```
GenerateOverlapMesh()
  for all faces f in FirstMesh
    OverlapPath p = GenerateOverlapPath(f)
    GenerateOverlapFaces(p, OverlapMesh)

GenerateOverlapPath(FirstFace)
```

```
527   OverlapPath = {}
528   CurrentNode = first node of FirstFace
529   CurrentSegment = line connecting CurrentNode to second node of FirstFace
530   Find SecondFace on SecondMesh from CurrentNode
531   for all edges e1 in FirstFace
532     while segments still remain in edge
533       for all edges e2 of SecondFace
534         if CurrentSegment intersects e2
535           determine intersection node NextNode
536           add new edge [CurrentNode, NextNode] to OverlapPath
537           update CurrentNode, CurrentSegment
538       if CurrentSegment does not intersect any edges of SecondFace
539         set next FirstFace edge
540         break segment loop

541 GenerateOverlapFaces(OverlapPath, OverlapMesh)
542   for all remaining edges e in OverlapPath
543     remove edge e from OverlapPath
544     if e intersects an edge on SecondMesh
545       follow SecondMesh edges until re-intersect with OverlapPath
546     else continue
547     if a closed element has been completed
548       add a new Face to OverlapMesh
549   add all Faces from SecondMesh interior to OverlapPath to OverlapMesh
```

References

Boyd, J. P., 2001: *Chebyshev and Fourier spectral methods*. Courier Dover Publications.

Boyd, S., and L. Vandenberghe, 2009: *Convex optimization*. Cambridge University Press.

Deville, M. O., P. F. Fischer, and E. H. Mund, 2002: *High-order methods for incompressible fluid flow*, Vol. 9. Cambridge University Press.

Dong, L., and B. Wang, 2013: Trajectory-tracking scheme in lagrangian form for solving linear advection problems: interface spatial discretization. *Monthly Weather Review*, **141 (1)**, 324–339.

Dukowicz, J. K., and J. W. Kodis, 1987: Accurate conservative remapping (rezoning) for arbitrary Lagrangian-Eulerian computations. *SIAM J. Sci. Stat. Comput.*, **8 (3)**, 305–321, doi:http://dx.doi.org/10.1137/0908037.

Dunavant, D., 1985: High degree efficient symmetrical gaussian quadrature rules for the triangle. *International Journal for Numerical Methods in Engineering*, **21 (6)**, 1129–1148.

Erath, C., P. H. Lauritzen, and H. M. Tufo, 2013: On mass conservation in high-order high-resolution rigorous remapping schemes on the sphere. *Mon. Weather Rev.*, **141 (6)**, 2128–2133.

Farrell, P., and J. Maddison, 2011: Conservative interpolation between volume meshes by local galerkin projection. *Computer Methods in Applied Mechanics and Engineering*, **200 (1–4)**, 89 – 100, doi:10.1016/j.cma.2010.07.015.

Farrell, P., M. Piggott, C. Pain, G. Gorman, and C. Wilson, 2009: Conservative interpolation between unstructured meshes via supermesh construction. *Computer Methods in Applied Mechanics and Engineering*, **198 (33)**, 2632–2642.

Guba, O., M. A. Taylor, P. A. Ullrich, J. R. Overfelt, and M. N. Levy, 2014: The spectral element method on variable resolution grids: Evaluating grid sensitivity and resolution-aware numerical viscosity. *Geosci. Model Dev. Discuss.*, submitted May 2014.

Hill, C., C. DeLuca, M. Suarez, A. da Silva, and Coauthors, 2004: The architecture of the earth system modeling framework. *Computing in Science & Engineering*, **6 (1)**, 18–28.

Jones, P. W., 1999: First- and second-order conservative remapping schemes for grids in spherical coordinates. *Mon. Weather Rev.*, **127**, 2204–2210.

Lauritzen, P. H., and R. D. Nair, 2007: Monotone and conservative cascade remapping between spherical grids (CaRS): Regular latitude-longitude and cubed-sphere grids. *Mon. Weather Rev.*, **136**, 1416–1432.

Lauritzen, P. H., R. D. Nair, and P. A. Ullrich, 2010: A conservative semi-Lagrangian multi-tracer transport scheme (CSLAM) on the cubed-sphere grid. *J. Comput. Phys.*, **229 (5)**, 1401–1424.

Margolin, L., and M. Shashkov, 2003: Second-order sign-preserving conservative interpolation (remapping) on general grids. *Journal of Computational Physics*, **184 (1)**, 266–298.

Nair, R. D., and B. Machenhauer, 2002: The mass-conservative cell-integrated semi-Lagrangian advection scheme on the sphere. *Mon. Weather Rev.*, **130 (3)**, 649–667.

Neale, R. B., and Coauthors, 2010: Description of the NCAR Community Atmosphere Model (CAM 5.0). NCAR Technical Note NCAR/TN-486+STR, National Center for Atmospheric Research, Boulder, Colorado. Available from http://www.cesm.ucar.edu/models/cesm1.0/cam/.

Ullrich, P. A., P. H. Lauritzen, and C. Jablonowski, 2009: Geometrically exact conservative remapping (GECoRe): Regular latitude-longitude and cubed-sphere grids. *Mon. Weather Rev.*, **137 (6)**, 1721–1741.

Ullrich, P. A., P. H. Lauritzen, and C. Jablonowski, 2013: Some considerations for high-order incremental remap-based transport schemes: edges, reconstructions, and area integration. *International Journal for Numerical Methods in Fluids*, **71 (9)**, 1131–1151.

Zarzycki, C. M., M. N. Levy, C. Jablonowski, J. R. Overfelt, M. A. Taylor, and P. A. Ullrich, 2014: Aquaplanet experiments using cam's variable resolution dynamical core. *Journal of Climate*, **27**, 5481–5503, doi:10.1175/JCLI-D-14-00004.1.

LIST OF FIGURES

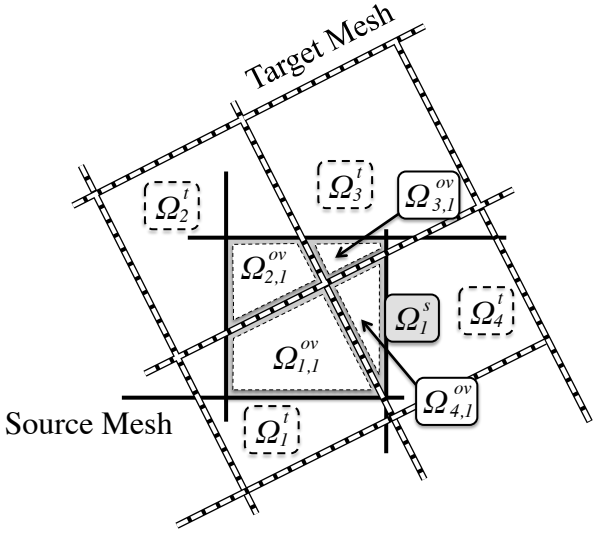

FIG. 1: A simplified depiction of a source mesh, target mesh and overlap mesh along with associated element indices. Region Ω_1^s is local with Ω_1^t, Ω_2^t, Ω_3^t and Ω_4^t.

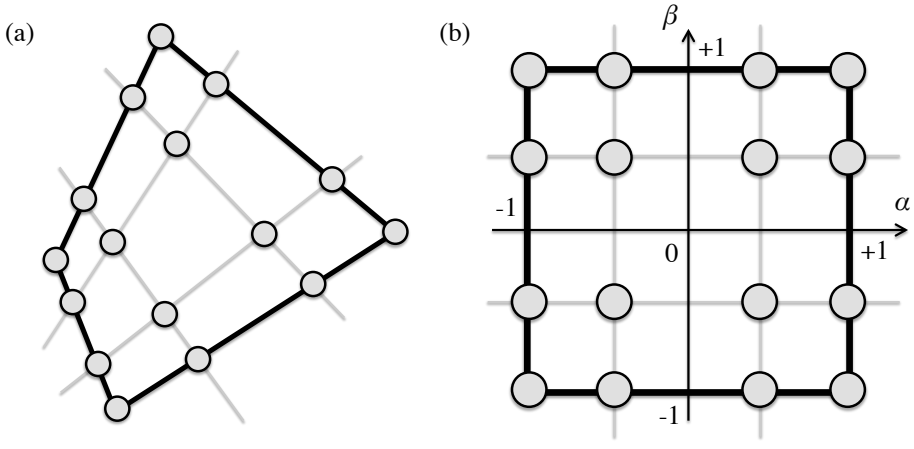

FIG. 2: (a) Geometric distribution of degrees of freedom in a fourth-order Gauss-Lobatto-Legendre finite element. (b) Degrees of freedom in the fourth-order Gauss-Lobatto-Legendre reference element, with coordinate axes $\alpha \in [-1,1]$ and $\beta \in [-1,1]$.

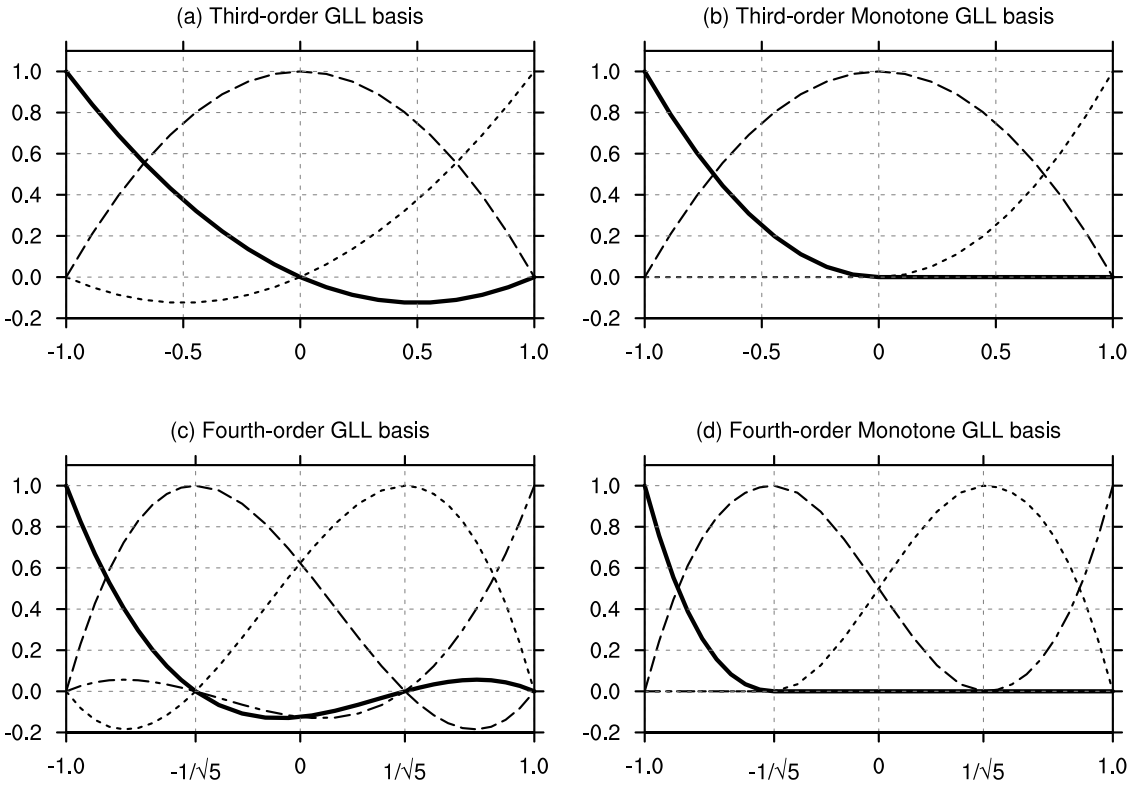

FIG. 3: Third- and fourth-order GLL basis functions used for the continuous reconstruction.

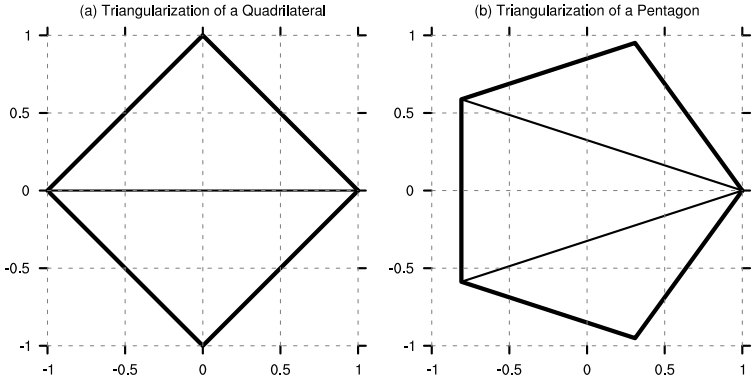

FIG. 4: Subdivision of a quadrilateral and pentagon into triangles.

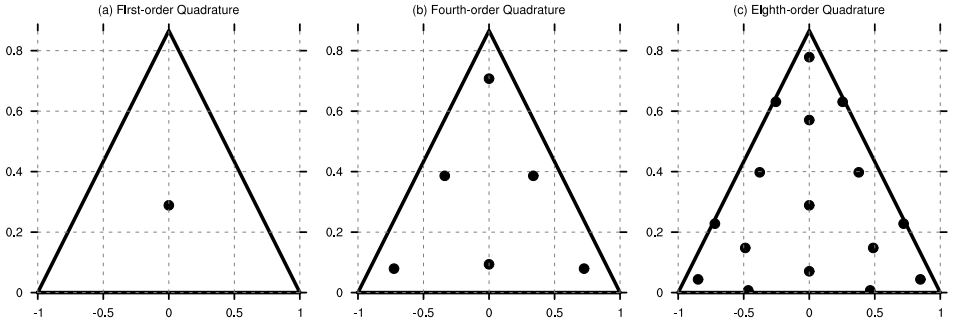

FIG. 5: First-, fourth- and eighth-order triangular quadrature nodes.

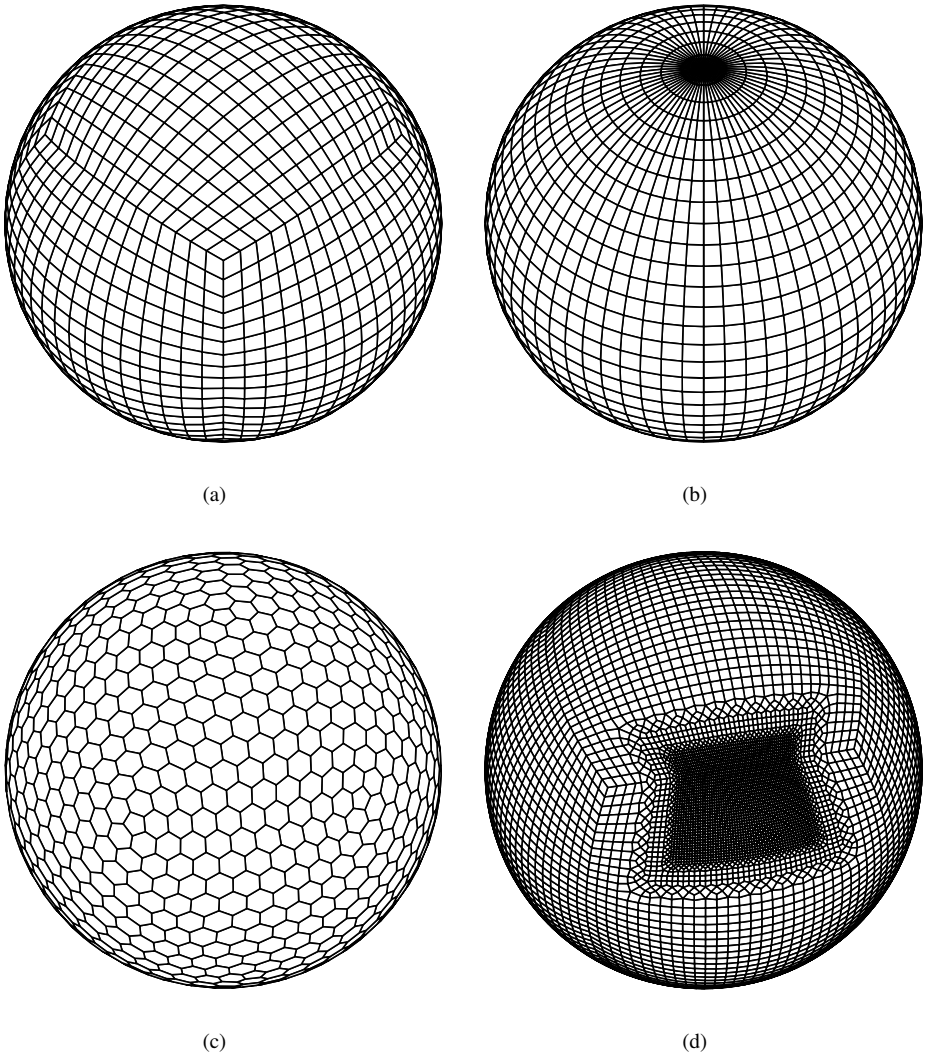

FIG. 6: A depiction of the four meshes studied in this manuscript: (a) Cubed-sphere, (b) Great-circle latitude-longitude, (c) Icosahedral / geodesic and (d) Refined cubed-sphere.

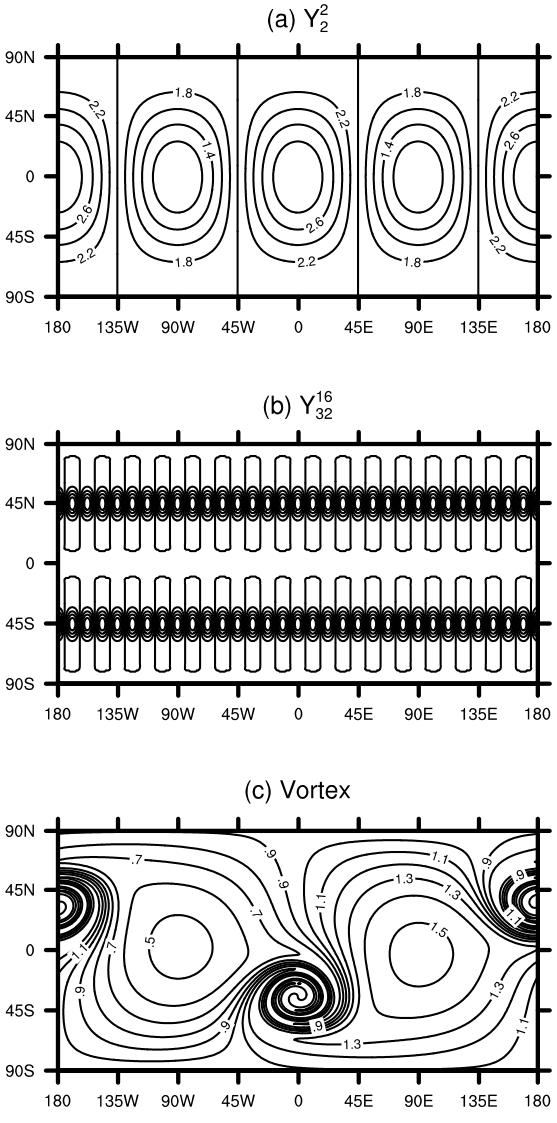

FIG. 7: Contour plots of the three test fields used in this study. Fields (a) and (b) take on values in the range [1,3]. Field (c) takes on values in the approximate range [0.46, 1.54].

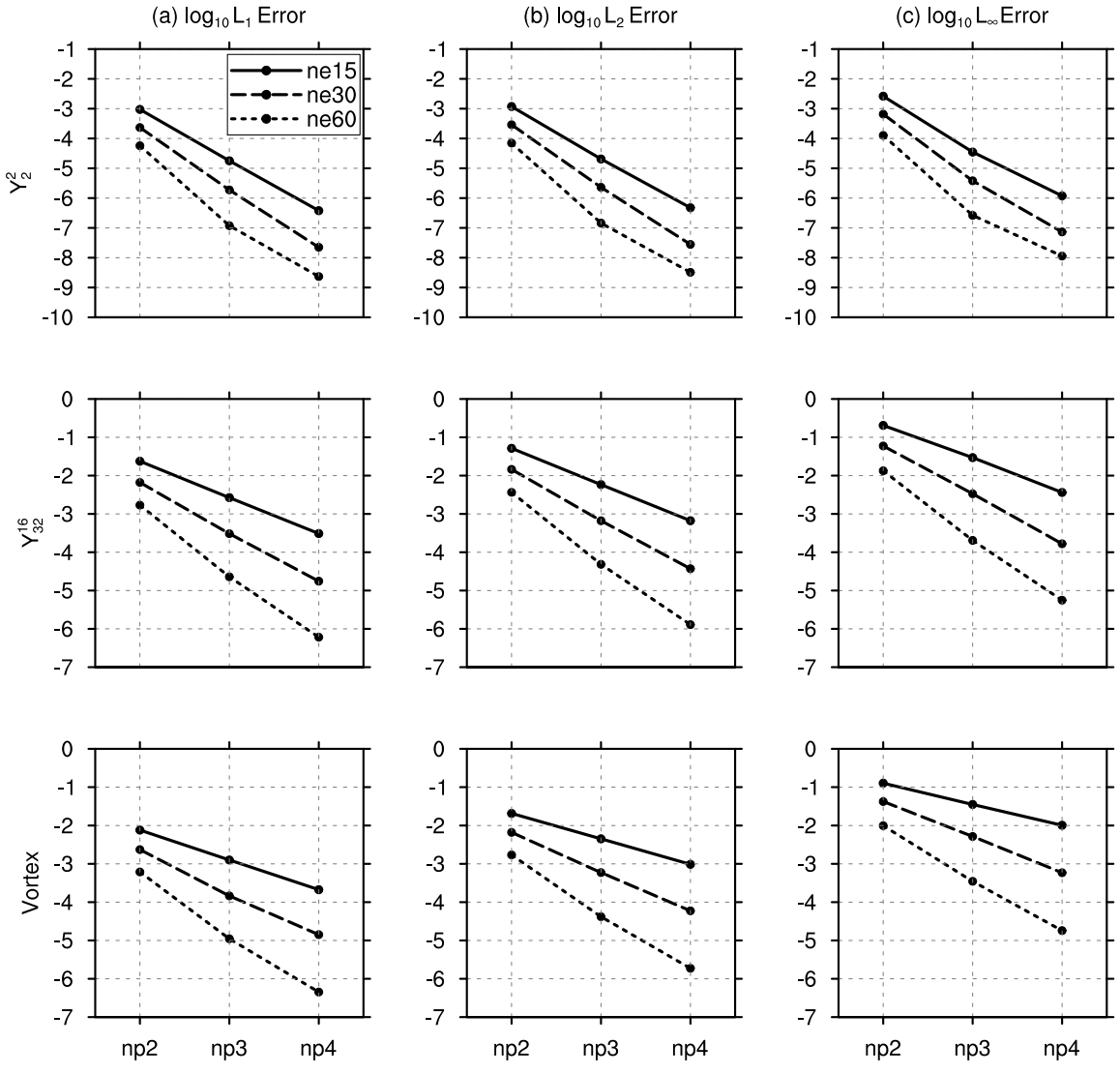

FIG. 8: Standard L_1, L_2 and L_∞ error norms reported for conservative and consistent remapping of the three idealized fields from the cubed-sphere mesh to the 1° great circle latitude-longitude mesh for cubed-sphere resolutions $n_e = 15, 30, 60$ and for three orders of accuracy $N_p = 2, 3, 4$.

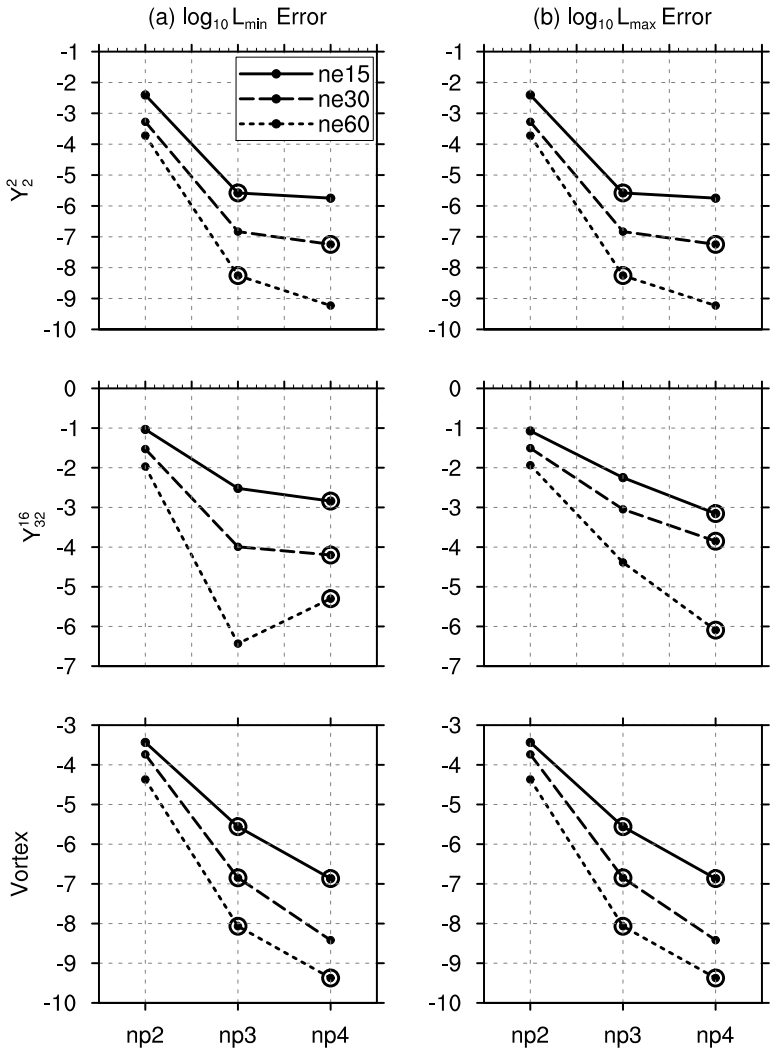

FIG. 9: Absolute L_{min} and L_{max} error norms reported for conservative and consistent remapping of the three idealized fields from the cubed-sphere mesh to the 1° great circle latitude-longitude mesh for cubed-sphere resolutions $n_e = 15, 30, 60$ and for three orders of accuracy $N_p = 2, 3, 4$. Circled data points indicate that the global minimum / maximum has been enhanced (*i.e.* that monotonicity was not maintained).

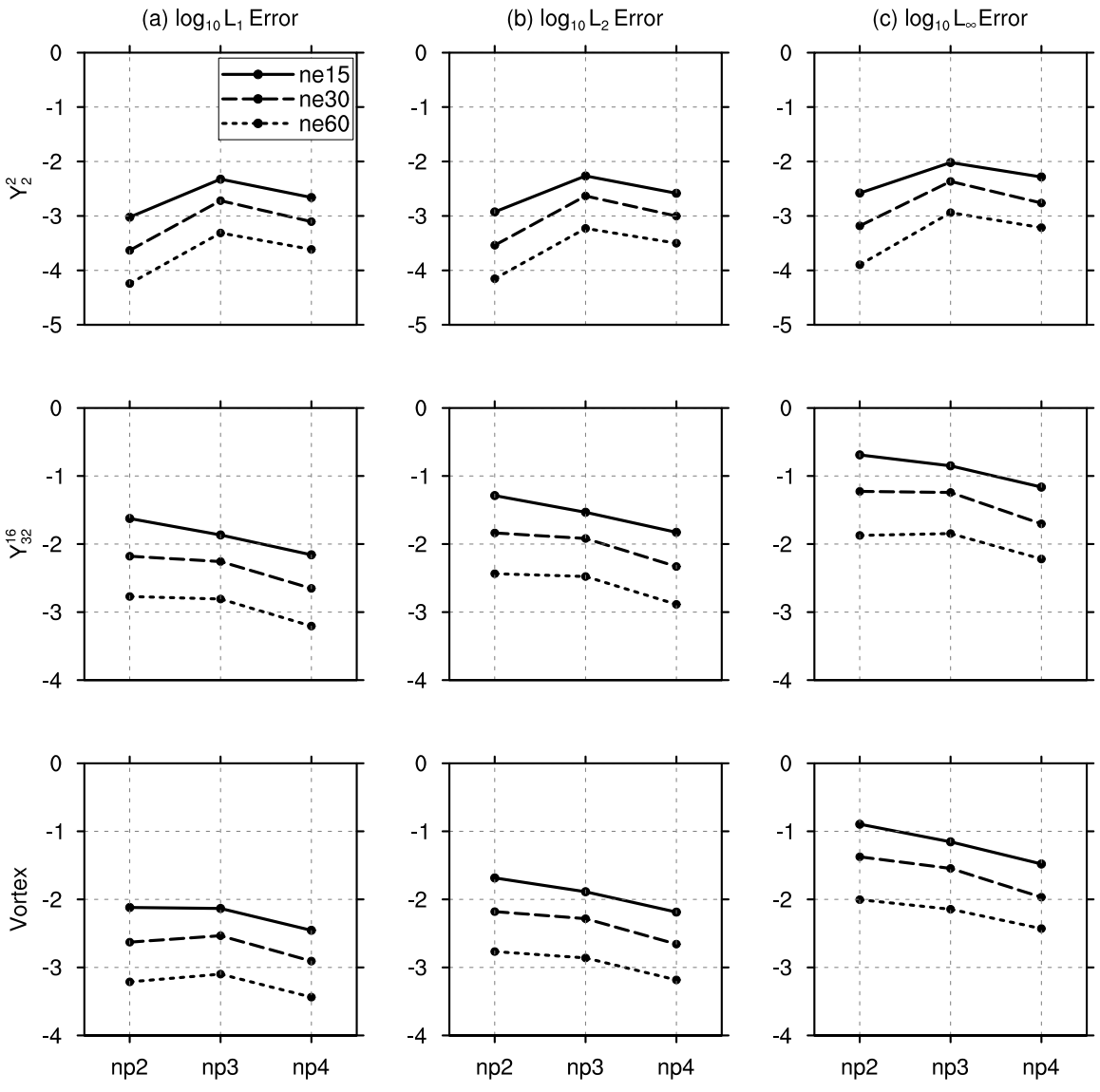

FIG. 10: Standard L_1, L_2 and L_∞ error norms reported for conservative, consistent and strictly monotonic remapping of the three idealized fields from the cubed-sphere mesh to the 1° great circle latitude-longitude mesh for cubed-sphere resolutions $n_e = 15, 30, 60$ and for three orders of accuracy $N_p = 2, 3, 4$.

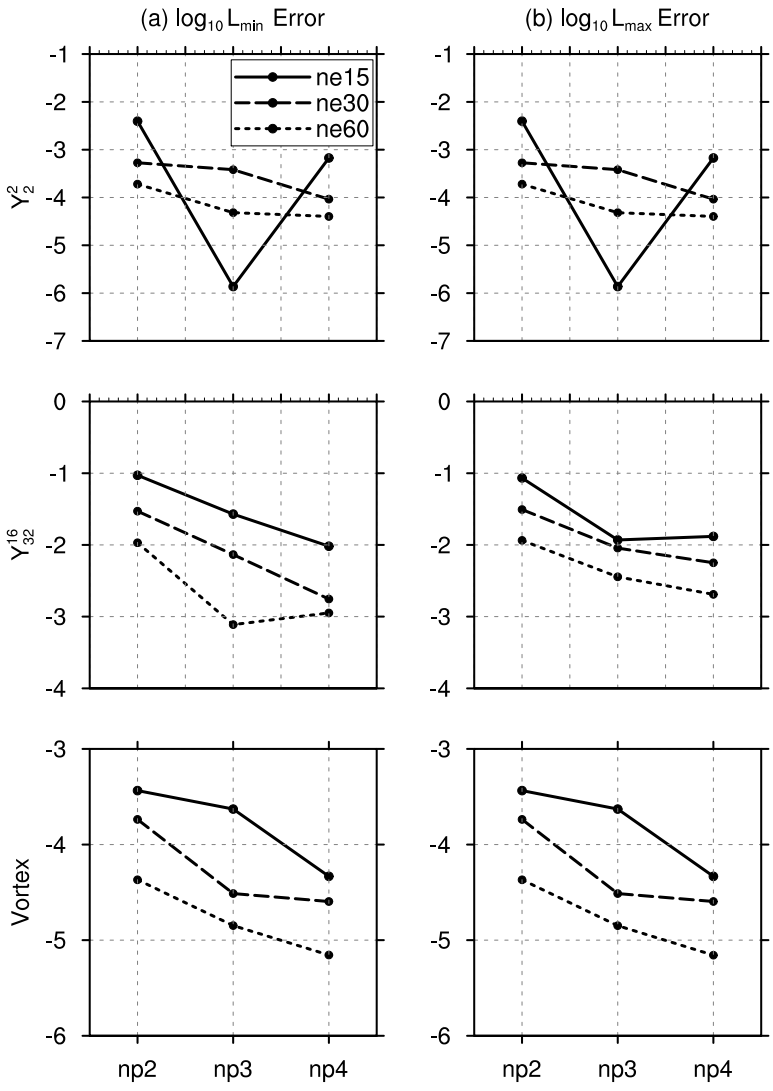

FIG. 11: Absolute L_{min} and L_{max} error norms reported for conservative, consistent and strictly monotonic remapping of the three idealized fields from the cubed-sphere mesh to the 1° great circle latitude-longitude mesh for cubed-sphere resolutions $n_e = 15, 30, 60$ and for three orders of accuracy $N_p = 2, 3, 4$.

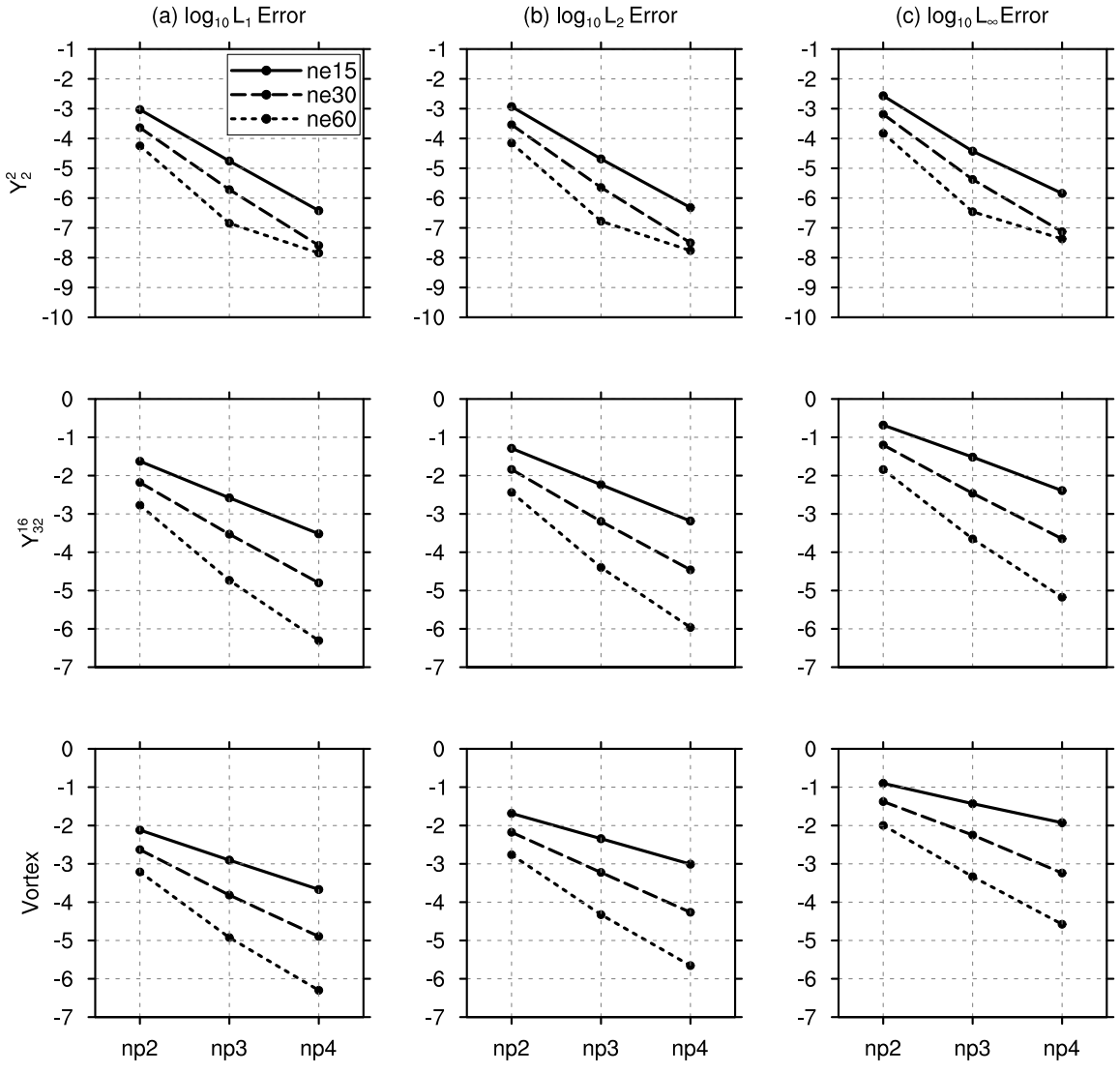

FIG. 12: Standard L_1, L_2 and L_∞ error norms reported for conservative and consistent remapping of the three idealized fields from the cubed-sphere mesh to the $N_i = 72$ geodesic mesh for cubed-sphere resolutions $n_e = 15, 30, 60$ and for three orders of accuracy $N_p = 2, 3, 4$.

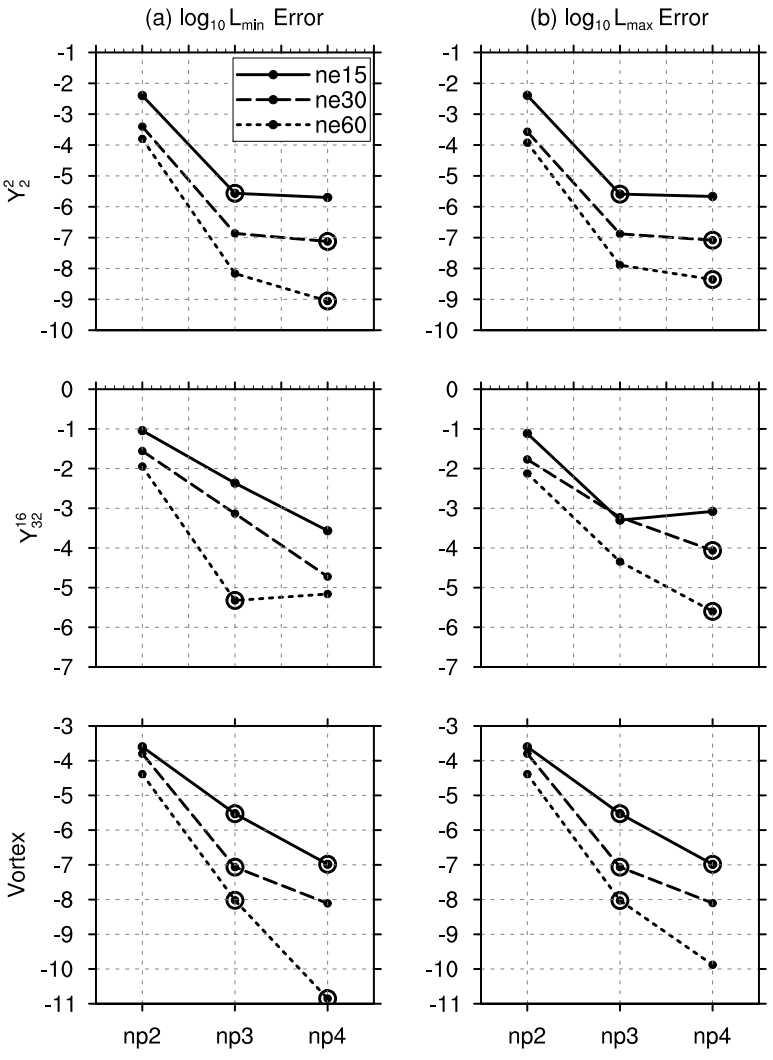

FIG. 13: Absolute L_{min} and L_{max} error norms reported for conservative and consistent remapping of the three idealized fields from the cubed-sphere mesh to the $N_i = 72$ geodesic mesh for cubed-sphere resolutions $n_e = 15, 30, 60$ and for three orders of accuracy $N_p = 2, 3, 4$.

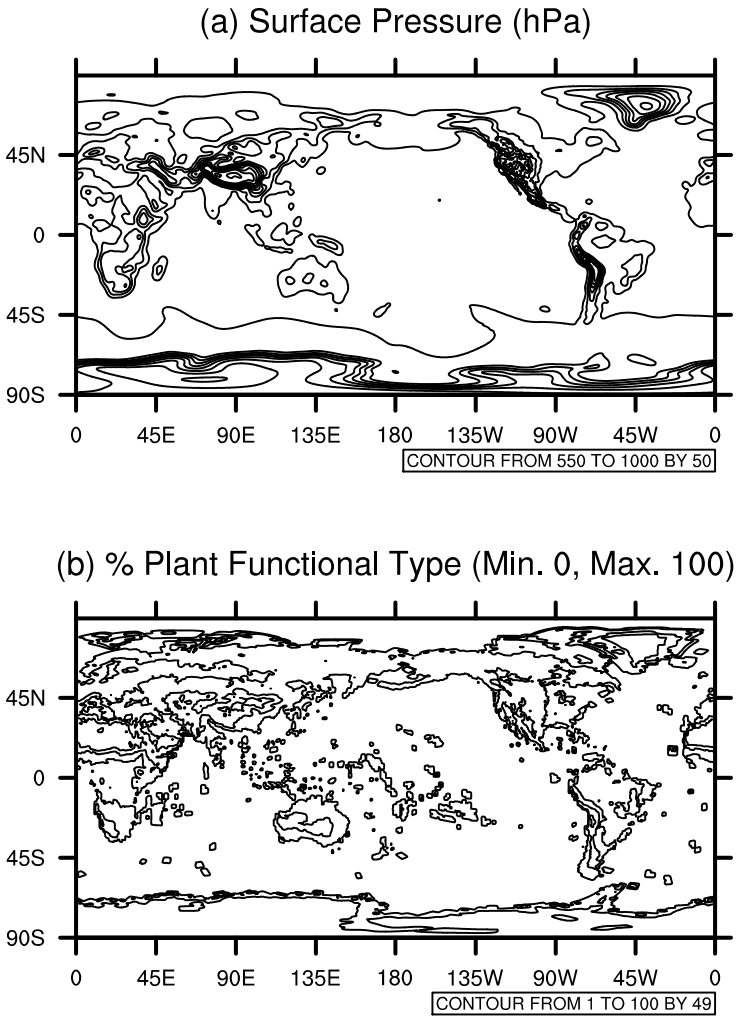

FIG. 14: Two "real data" tests for remapping from the variable resolution cubed-sphere mesh (Figure 6d) with $N_p = 4$ to a 0.25° great circle latitude-longitude grid (Figure 6b). (a) Surface pressure from a variable resolution simulation using conservative and consistent remapping. Observe that the detail of the result is much finer between 135W and 90W in the Northern hemisphere, corresponding to the region of highest mesh refinement. (b) Percentage plant functional type (barren land) using conservative, consistent and monotone remapping. This field is highly discontinuous and requires that the data be constrained to the interval $[0, 100]$ to be considered meaningful.